The first high-redshift changing-look quasars

Nicholas P. Ross[1]★, Matthew J. Graham[2], Giorgio Calderone[3], K. E. Saavik Ford[4,5,6], Barry McKernan[4,5,6] and Daniel Stern[7]

[1]*Institute for Astronomy, University of Edinburgh, Royal Observatory, Blackford Hill, Edinburgh EH9 3HJ, United Kingdom*

[2]*Cahill Center for Astronomy and Astrophysics, California Institute of Technology, Mail Code 249/17, 1200 E California Blvd, Pasadena CA 91125, USA*

[3]*INAF – Osservatorio Astronomico di Trieste, Via Tiepolo 11, I-34143 Trieste, Italy*

[4]*Department of Science, BMCC, City University of New York, New York, NY 10007, USA*

[5]*Department of Astrophysics, Rose Center for Earth and Space, American Museum of Natural History, Central Park West at 79th Street, NY 10024, USA*

[6]*Graduate Center, City University of New York, 365 5th Avenue, New York, NY 10016, USA*

[7]*Jet Propulsion Laboratory, California Institute of Technology, 4800 Oak Grove Drive, Mail Stop 169-221, Pasadena, CA 91109, USA*

ABSTRACT

We report on three redshift $z > 2$ quasars with dramatic changes in their C IV emission lines, the first sample of changing-look quasars (CLQs) at high redshift. This is also the first time the changing-look behaviour has been seen in a high-ionisation emission line. SDSS J1205+3422, J1638+2827, and J2228+2201 show interesting behaviour in their observed optical light curves, and subsequent spectroscopy shows significant changes in the C IV broad emission line, with both line collapse and emergence being displayed on rest-frame timescales of ~240-1640 days. These are rapid changes, especially when considering virial black hole mass estimates of $M_{BH} > 10^9 M_\odot$ for all three quasars. Continuum and emission line measurements from the three quasars show changes in the continuum-equivalent width plane with the CLQs seen to be on the edge of the full population distribution, and showing indications of an intrinsic Baldwin effect. We put these observations in context with recent state-change models, and note that even in their observed low-state, the C IV CLQs are generally above ~5% in Eddington luminosity.

Key words: accretion, accretion discs – surveys – quasars: general – quasars: time-domain – quasars: individual (SDSS J120544.7+342252.4, SDSS J163852.9+28270.7.7, SDSS J222818.7+220102.9)

1 INTRODUCTION

Luminous AGN, i.e. quasars, are now seen to significantly vary their energy output on timescales as short as weeks to months. This observation, and the subsequent mismatch in the expected viscous timescale, which for a $10^7 M_\odot$ central supermassive black hole (SMBH) is ~hundreds of years, was noted over 30 years ago (e.g. Alloin et al. 1985). However, with new photometric light-curve and repeat spectroscopic data, the desire for a deeper understanding of AGN accretion disk physics has recently re-invigorated the field (e.g., Antonucci 2018; Lawrence 2018; Ross et al. 2018; Stern et al. 2018).

The optical continuum variability of quasars was recognised since their first optical identifications (Matthews & Sandage 1963). **However, dramatic changes** in the broad emission lines (BELs) of quasars was only recently first identified (LaMassa et al. 2015). Samples of over 100 "changing-look" quasars (CLQs) or "changing-state" quasars (CSQs) have now been assembled (e.g., MacLeod et al. 2019; Graham et al. 2020). The community uses both these

terms as a cover for the underlying physics. For sake of argument, CLQs can potentially be thought of as the extension to the BELs of quasar continuum variability (e.g., MacLeod et al. 2012) whereas the CSQs have a state-transition, perhaps similar to that seen in Galactic X-ray binaries (Noda & Done 2018; Ruan et al. 2019). In this paper, we use the term "changing-look", as we are currently agnostic, and confessedly ignorant, to the underlying physical processes.

CLQs to date have primarily been defined according to the (recombination) Balmer emission line properties with particular attention paid to the Hβ emission line, observed from optical spectroscopy. Recent works report on discoveries of Mg II changing-look AGN (Guo et al. 2019; Homan et al. 2019). However, current CLQ studies have primarily been at redshifts $z < 1$.

While there have been many studies on triply ionised carbon, i.e., C IV, these have tended to focus on broad absorption line quasars (e.g., Table 1 of Hemler et al. 2019) or the Baldwin effect (Baldwin 1977; Bian et al. 2012; Jensen et al. 2016; Hamann et al. 2017)[1].

★ E-mail: npross@roe.ac.uk

[1] As noted in Rakić et al. (2017), two different types of Baldwin effect

[margin annotation: I think it would be nice to keep this table, but I agree dropping would not compromise the overall presentation. Hence, I would leave the final decision to the Editor, stating that we have simply a preference in retaining it.]

Line	λ / Å	Transition Energy / eV	Ionisation Energy / eV	Lower			Upper			Wavenumber / cm^{-1}	$A_{i,j}$ / 10^8 s^{-1}	Physical Mechanism
H LyLim	912.324	13.5984	13.5984	$1s$	^{2}S	1/2	∞			109 678.7	1.23×10^{-6}	Ionisation
H Lyα	1215.670	10.1988	13.5984	$1s$	^{2}S	1/2	2			82 259.2	4.67	Recombination
N v	1238.821	10.0082	97.8901	$1s^22s$	^{2}S	1/2	$1s^22p$	^{2}P^o	3/2	80 721.9	3.40	Collisional
N v	1242.804	9.9762	97.8901	$1s^22s$	^{2}S	1/2	$1s^22p$	^{2}P^o	1/2	80 463.2	3.37	Collisional
C iv	1548.187	8.0083	64.4935	$1s^22s$	^{2}S	1/2	$1s^22p$	^{2}P^o	3/2	64 591.7	2.65	Collisional
C iv	1550.772	7.9950	64.4935	$1s^22s$	^{2}S	1/2	$1s^22p$	^{2}P^o	1/2	64 484.0	2.64	Collisional
He ii	1640.474	7.5578	54.4178	$2p$	^{2}P^o	3/2	$3d$	^{2}D	5/2	60 958.0	10.35	Recombination
He ii	1640.490	7.5578	54.4178	$2p$	^{2}P^o	3/2	$3d$	^{2}D	3/2	60 957.4	1.73	Recombination
C iii]	1906.683	6.5026	47.8878	$1s^22s^2$	^{1}S	0	$1s^22s2p$	^{3}P^o	2	52 447.1	5.19×10^{-11}	Collisional
C iii]	1908.734	6.4956	47.8878	$1s^22s^2$	^{1}S	0	$1s^22s2p$	^{3}P^o	1	52 390.8	1.14×10^{-6}	Collisional
Mg ii	2795.528	4.4338	15.0353	$2p^63s$	^{2}S	1/2	$2p^63p$	^{2}P^o	3/2	35 760.9	2.60	Collisional
Mg ii	2802.705	4.4224	15.0353	$2p^63s$	^{2}S	1/2	$2p^63p$	^{2}P^o	1/2	35 669.3	2.57	Collisional
H Ba β	4861.333	2.5497	13.5984	2			4			20 564.8	0.0842	Recombination

Table 1. Strong UV/optical spectral emission lines in quasars, and their atomic data from the NIST Atomic Spectra Database (Kramida et al. 2018; Kramida et al. 2019). The transition energies are $E = hc/\lambda$ for the given wavelength. The ionisation energy is the energy required to ionise the given species, e.g., 64.49 eV is needed to create a C v ion. Transition level configurations are given in standard spectroscopic notation, with $A_{i,j}$ denoting the transition probabilities. **The physical mechanism for the generation of the emission lines e.g., full ionization, collisionally excitation or recombination are also given** *[margin annotation: in the last column.]*

Dramatic changes in the collisionally excited broad *emission* line of C iv — and indeed C iii] — have not to this point been reported.

Here, we present new results for three quasars which show dramatic changes in their C iv and C iii] broad emission line properties and underlying continuum. These are some of the first examples of CLQs at high ($z > 1$) redshift. Moreover, these are the first cases for substantial changes of ions with high ionisation potentials (I.P.'s >2 Rydberg), thus linking the ionizing photons to the energetic inner accretion disk.

Details of the atomic transitions that produce strong rest-frame UV/optical lines in quasars are given in Table 1. **Table 1 also gives the physical mechanisms producing these emission lines.**

Most of the strong lines in the near-UV spectrum are collisionally excited, including the the C iv 1548. *[annotation: (47.89 ev, or 3.519Ry)]* **The He ii 1640 recombination line is among the exceptions. The relevant ionization potential is that of the doubly-ionised C iii ion, i.e., it the photon energy needed to** *create the C iv ion.* ~~47.89 eV (3.519 Ry) is required for C iii to create triply-ionised C iv.~~ **The ionization potential** ~~of the C iv ion~~ **to create** ~~C v~~ *[annotation: next ionization level (Cv)]* **is 64.49 eV. The ionization potential** ~~of the N iv N IV ion~~ **to create N v is 77.46 eV, while** ~~the ionization potential of the N v ion to create~~ **N vi** *[annotation: creating / requires]* ~~is 97.89 eV~~**. Observing N v thus implies photons with** ~~gies~~ **of 98 eV are present in order to produce the ions that then emit the observed emission lines in the rest-frame UV spectral range.** *[annotation: Why?? Isn't it ~78eV, as suggested by the Referee?]*

In this paper we use the wavelengths of 1548.202 and 1550.774 Å for the C iv doublet (Kramida et al. 2018). For ionisation energies, 47.89 eV (3.519 Ry) is required for doubly-ionised C iii to become triply-ionised C iv, and 64.49 eV (4.74 Ry) is needed to ionise C iv itself. This energy corresponds to a thermal temperature of $T \gtrsim 4\times10^5$ K, implying a heating energy source of (soft) X-ray photons.

Wilhite et al. (2006) examine C iv variability in a sample of 105 quasars observed at multiple epochs by the Sloan Digital Sky Survey (SDSS; York et al. 2000; Stoughton et al. 2002; Abazajian

et al. 2009a). They find a strong correlation between the change in the C iv line flux and the change in the line width, but no correlations between the change in flux and changes in line center or skewness. These authors find that the relation between line flux change and line width change is consistent with a model in which a broad line base varies with greater amplitude than the line core. The C iv lines in these high-luminosity quasars appear to be less responsive to continuum variations than those in lower luminosity AGN.

Richards et al. (2011) explored the broad emission line region in over 30,000 $z > 1.54$ SDSS quasars, concentrating on the properties of the C iv emission line. These authors consider two well-known effects involving the C iv emission line: *(i)* the anti-correlation between the C iv equivalent width (EW) and luminosity (i.e., the Baldwin effect) and *(ii)* the blueshifting of the peak of C iv emission with respect to the systemic redshift. We denote the velocity offset of emission lines as V_{off} and use the convention that a positive V_{off} value means the line is blueshifted while a negative V_{off} value means the line is redshifted. Richards et al. (2011) find a blueshift of the C iv emission line is nearly ubiquitous, with a mean shift of $\langle V_{off}\rangle_{RQ} \sim 810$ km s^{-1} for radio-quiet (RQ) quasars and $\langle V_{off}\rangle_{RL} \sim 360$ km s^{-1} for radio-loud (RL) objects. Richards et al. (2011) also find the Baldwin effect is present in both their RQ sample and their RL sample. They conclude that these two C iv parameters (EW and blueshift) are capturing an important trade-off between disk and wind components in the disk-wind model of accretion disks (e.g., Murray et al. 1995; Elvis 2000; Proga et al. 2000; Leighly 2004), with one dominating over the other depending on the shape of the quasar spectral energy distribution (SED).

Using the multi-epoch spectra of 362 quasars from the SDSS Reverberation Mapping project (SDSS-RM; Shen et al. 2015, 2019), Sun et al. (2018) investigate the blueshift of C iv emission relative to Mg ii emission, and its dependence on quasar properties. They confirm that high-blueshift sources tend to have low C iv EWs, and that the low-EW sources span a range of blueshift. Other high-ionisation lines, such as He ii, also show similar blueshift properties. The ratio of the line width of C iv to that of Mg ii increases with blueshift. Sun et al. (2018) also find that quasar variability might slightly enhance the connection between the C iv blueshift and EW, though further investigation here is warranted. They also find that quasars with the largest blueshifts are less variable and tend to have higher Eddington ratios, though Eddington ratio alone might be an

are present in the literature: *(i)* the *global* (or *ensemble*) Baldwin effect, which is an anti-correlation between the emission line equivalent width and the underlying continuum luminosity of *single-epoch* observations of a *large number* of AGN, and *(ii)* the *intrinsic* Baldwin effect, the same anti-correlation but in an *individual, variable* AGN (Pogge & Peterson 1992).

Object	Redshift	g-band / mag	MJD	Instrument	Exposure time / sec	SDSS Plate-FiberID	Notes
J120544.7+342252.4	2.068	18.27	53498	SDSS	8057	2089-427	Plate quality marginal
	2.071		58538	DBSP	1800	—	Poor conditions
	2.071		58693	DBSP	2400	—	Good conditions
J163852.9+282707.7	2.185	19.77	54553	SDSS	4801	2948-614	Plate quality good
	2.186		55832	BOSS	3600	5201-178	Plate quality good
	2.182		58583	LRIS	1800	—	
J222818.7+220102.9	2.217	19.97	56189	BOSS	2700	6118-720	Plate quality good
	2.222		56960	eBOSS	4500	7582-790	Plate quality good
	2.222		58693	DBSP	2400	—	

Table 2. Details of our spectroscopic observations. Redshift errors are typically ±0.002. SDSS, BOSS, and eBOSS spectra have resolving power $\mathcal{R} \equiv \lambda / \Delta\lambda \sim$ 2000. DBSP: Double Spectrograph on the Palomar 200-inch Hale telescope. LRIS: Low Resolution Imaging Spectrometer on Keck I 10-m telescope.

insufficient condition for the C IV blueshift. Recent investigations also include Meyer et al. (2019) and Doan et al. (2019). Dyer et al. (2019) provide a detailed analysis of 340 quasars at high redshift ($1.62 < z < 3.30$) from the SDSS-RM project, which we compare with our results in Section 4.2.

The purpose of this paper is, for the first time, to systematically access and report on the CLQ phenomenon at high ($z > 2$) redshift. While accessing this phenomenon at an earlier cosmic epoch is somewhat interesting, the main value of this study is to move from the low-ionisation energy Balmer emission line series at rest-frame optical wavelengths to the high-ionisation emission lines, in particular C IV λ1549, at rest-frame UV wavelengths.

This paper is organised as follows. In Section 2, we describe our sample selection, catalogues, and observational data sets. Section 3 presents the high-redshift quasars and reports their time-variable line properties. We provide a brief theoretical discussion in Section 4, and Section 5 presents our conclusions. We report all magnitudes on the AB zero-point system (Oke & Gunn 1983; Fukugita et al. 1996) unless otherwise stated. For the *WISE* bands, $m_{AB} = m_{Vega} + m$ where $m = 2.699$ and 3.339 for *WISE* W1 (3.4μm) and W2 (4.6μm), respectively (Cutri et al. 2011; Cutri 2013). We adopt a flat ΛCDM cosmology with $\Omega_\Lambda = 0.73$, $\Omega_M = 0.27$, and $h = 0.71$. All logarithms are to the base 10.

2 CLQ SELECTION AND LINE MEASUREMENTS

In this section we present the photometric data used to select the CLQs and give details of the multiwavelength data where we have it. **We use data from the Catalina Real-time Transient Survey, PanSTARRS, the Zwicky Transient Facility, the WISE mission and SDSS. By design our data sources and overall methodology, are in common to the recent Ross et al. (2018), Stern et al. (2018) and Graham et al. (2020) papers.** We then give details of the spectroscopic data including emission lines measurements.

2.1 Photometry

2.1.1 Optical Photometry

We use optical data from the Catalina Real-time Transient Survey (CRTS; Drake et al. 2009; Mahabal et al. 2011), the Panoramic Survey Telescope and Rapid Response System (PanSTARRS; Kaiser et al. 2010; Stubbs et al. 2010; Tonry et al. 2012; Magnier et al. 2013), and the Zwicky Transient Facility (ZTF; Bellm et al. 2019a).

The CRTS archive[2] contains the Catalina Sky Survey data streams from three telescopes – the 0.7-m Catalina Sky Survey (CSS) Schmidt and 1.5-m Mount Lemmon Survey (MLS) telescopes in Arizona, and the 0.5-m Siding Springs Survey (SSS) Schmidt in Australia. CRTS covers up to ~2500 deg^2 per night, with four exposures per visit, separated by 10 min. The survey observes over 21 nights per lunation. The data are broadly calibrated to Johnson V (for details, see Drake et al. 2013) and the current CRTS data set contains time series for approximately 400 million sources to $V \sim 20$ above Dec > -30 from 2003 to 2016 May (observed with CSS and MLS) and 100 million sources to $V \sim 19$ in the southern sky from 2005 to 2013 (from SSS). CRTS has been extensively used to study quasar variability (e.g., Graham et al. 2014, 2015a,b, 2017, 2020; Stern et al. 2017, 2018; Ross et al. 2018).

PanSTARRS data is obtained via the Pan-STARRS Catalog Search interface[3]. We query the PS1 DR2 Detection catalog.

The Zwicky Transient Facility (ZTF; http://ztf.caltech.edu) is a new robotic time-domain sky survey capable of visiting the entire visible sky north of -30 declination every night. ZTF observes the sky in the g, r, and i-bands at different cadences depending on the scientific program and sky region (Bellm et al. 2019b; Graham et al. 2019). The ZTF 576 megapixel camera with a 47 deg^2 field of view, installed on the Samuel Oschin 48-inch Schmidt telescope at Palomar observatory, can scan more than 3750 deg^2 per hour, to a 5σ detection limit of 20.7 mag in the r-band with a 30-sec exposure during new moon (Masci et al. 2019).

2.1.2 Mid-Infrared Photometry

Mid-infrared data (3.4 and 4.6μm) is available from the beginning of the *WISE* mission (2010 January; Wright et al. 2010) through the fifth-year of *NEOWISE-R* operations (2018 December; Mainzer et al. 2011). The *WISE* scan pattern leads to coverage of the full-sky approximately once every six months (a "sky pass"), albeit it with a gab between 2011 February and 2013 October when the satellite was placed in hibernation. Hence, our light curves have a cadence of 6 months with a 32-month sampling gap.

2.2 CLQ Selection

Our high-redshift CLQs were identified as follows. We selected all 64,774 SDSS DR15 sources with $z > 0.35$ classified as 'quasar',

---

[2] http://catalinadata.org
[3] https://catalogs.mast.stsci.edu/panstarrs/
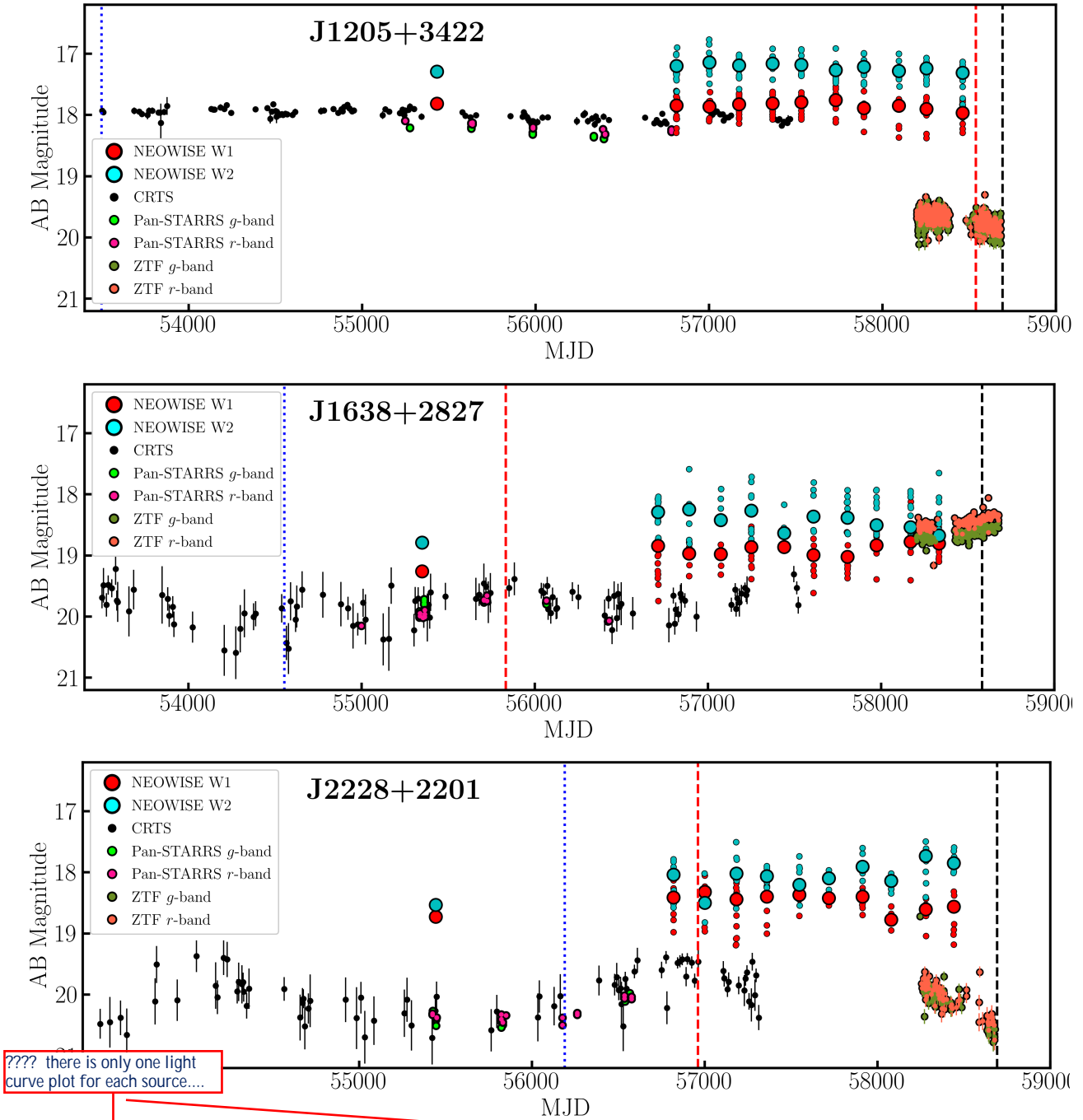
Figure 1. The three high-redshift CLQ quasars; J1205+3422 (top), J1638+2827 (middle) and J2228+2201 (bottom). The light curve data are presented in the panels on the left hand side, with the timing of the spectral observations indicated with vertical dashed lines. The spectra are on the right hand side, with zoom-in's on the Lyα-N v complex, the C iv line, and the Mg ii line.

that had at least two spectra separated by ≥ 100 days, and that had a corresponding CRTS light curve. We fitted a damped random walk to the CRTS data via Gaussian process regression (using the GPy Python library). This allowed us to predict the photometric magnitudes at the epochs of the SDSS spectra for each source. This allowed us to predict the photometric magnitudes at the epochs of the SDSS spectra for each source. **TO DO MJG:: "I presume that the damped random walk model was used to INTERPO-LATE between adjacent points in the light cure. If so, it would be useful to state that explicitly. It would also be useful to note**

the uncertainty in this int[...] **important in developing a**[...] **authors do."** Those with |Δ[...] inspection, looking for at least a 50% change in magnitude between the two epochs. **"I would recommend elaborating on this matter by explaining why the specific criterion of |DV| > 0.3 was adopted (by the way, what are the units? magnitudes?)"** The specific criterion of $|\Delta V| > 0.3$ was adopted since... **(ii) In the next sentence, what does "looking for at least a 50% change in magnitude between the two epochs" mean? I presume the authors**
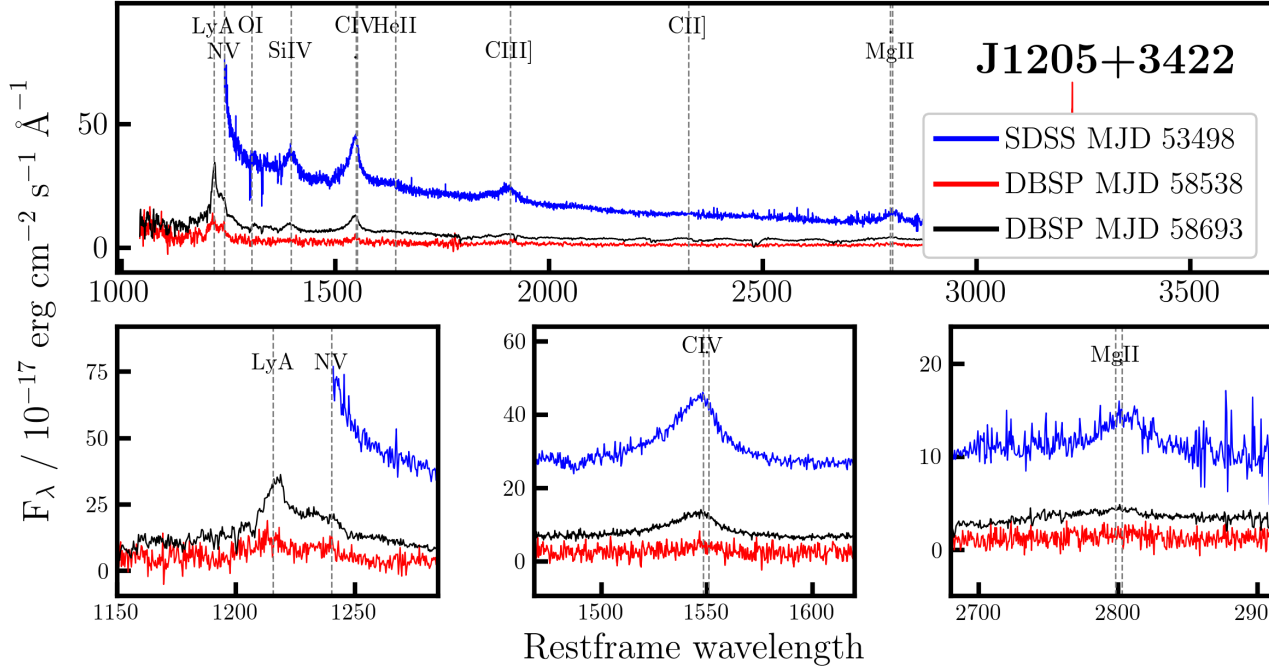
Figure 2. The three epochs of spectra for SDSS J1205+3422. The full wavelength spectrum is presented in the top panel, with zoom-in's on the Lyα-N v complex, the C IV line, and the Mg II line in the lower panels
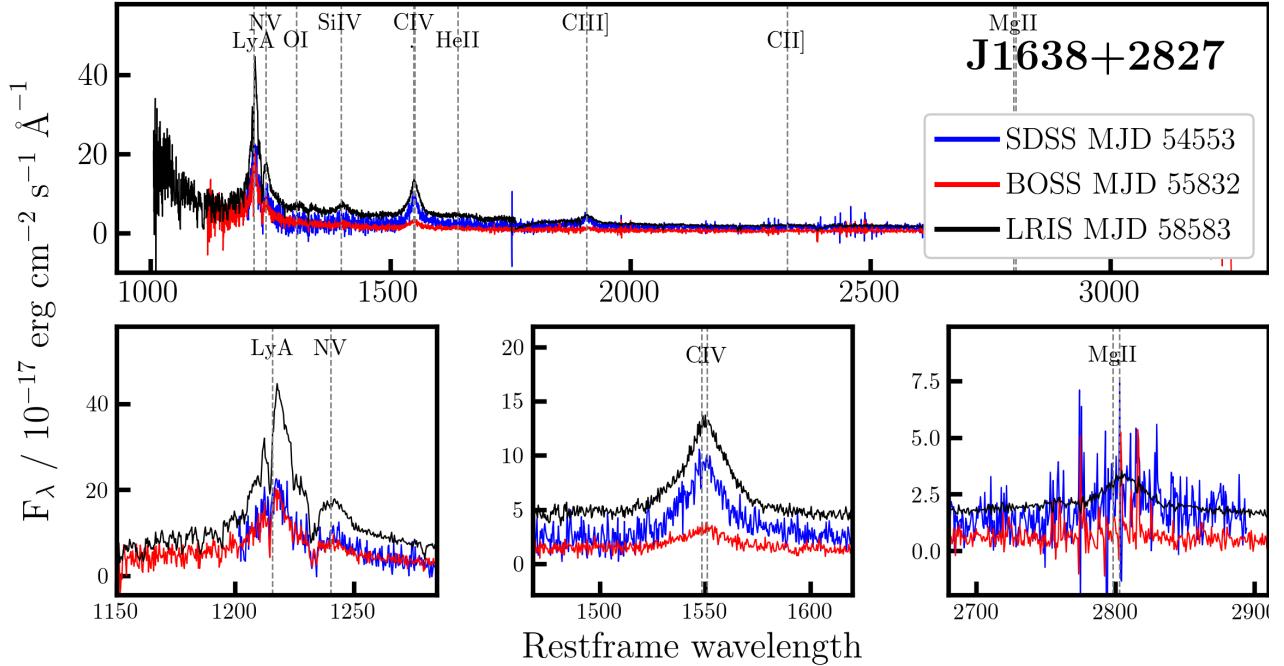
Figure 3. As Figure 2 but for J1638+2827.

looked for a fractional difference in FLUX, not MAGNITUDE (a 50% difference in magnitude is not a well-defined measure of variability). (iii) Finally, I would suggest noting how many quasars were selected for visual inspection by the automatic algorithm before the three final candidates were identified.

Only three quasars, SDSS J120544.7+342252.4 (hereafter J1205+3422), SDSS J163852.93+282707.7 (hereafter J1638+2827) and SDSS J222818.76+220102.9 (hereafter J2228+2201), satisfied

these selection criteria and showed interesting or dramatic emission line behaviour.

2.3 Spectroscopy

An overview of our spectroscopic observations is given in Table 2. The archival spectra are from the SDSS (Stoughton et al. 2002; Abazajian et al. 2009b; Schneider et al. 2010), the SDSS-III Baryon Oscillation Spectroscopic Survey (BOSS; Eisenstein et al. 2011;
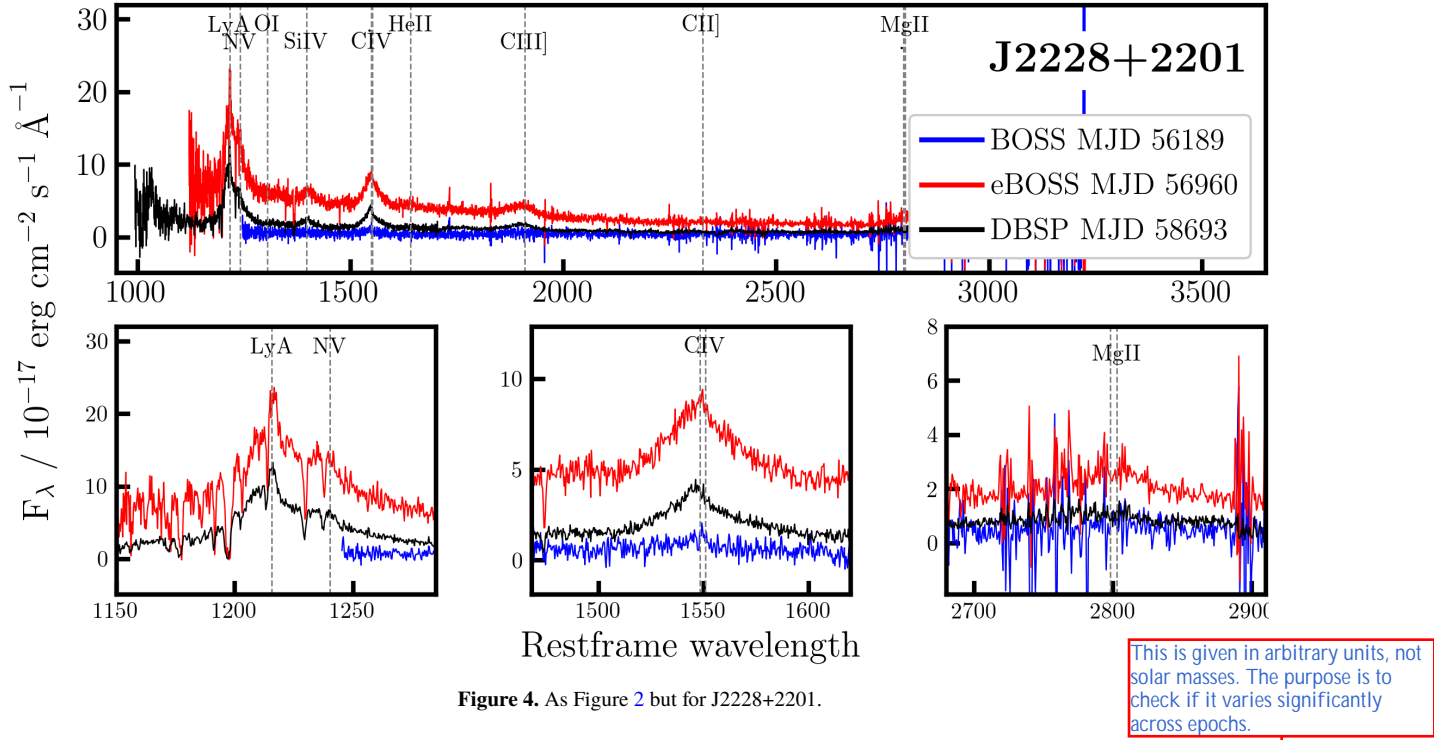
Figure 4. As Figure 2 but for J2228+2201.

This is given in arbitrary units, not solar masses. The purpose is to check if it varies significantly across epochs.

| Object | MJD | Cont. @ 1450Å | | CIV 1549Å | | | | Virial product |
		νL_ν 10^{42} erg s^{-1}	Slope (F$_\lambda \propto \lambda^\alpha$)	Luminosity 10^{42} erg s^{-1}	FWHM km s^{-1}	V_{off} km s^{-1}	EW Å	$\log(\nu L_\nu^{0.5} \times \text{FWHM}^2)$ ~~$\log(M/M_\odot)$~~
	53498	38130 ± 40	-1.57 ± 0.01	898 ± 15	6024 ± 120	944 ± 33	38 ± 1	9.85 ± 0.02
J1205+3422	58538*	2730 ± 40	-1.27 ± 0.05	161 ± 22	15000 ± 2500	922 ± 690	92 ± 13	10.07 ± 0.13
	58693	8550 ± 10	-1.41 ± 0.01	386 ± 4	7110 ± 90	1085 ± 29	71 ± 1	9.67 ± 0.01
	54553	3580 ± 50	-1.16 ± 0.07	294 ± 9	4630 ± 180	183 ± 57	128 ± 4	9.11 ± 0.04
J1638+2827	55832	2340 ± 20	-2.17 ± 0.05	85 ± 4	4730 ± 290	172 ± 89	60 ± 3	9.04 ± 0.05
	58583	7800 ± 20	-2.02 ± 0.01	368 ± 4	4510 ± 71	94 ± 24	78 ± 1	9.25 ± 0.01
	56189*	610 ± 50	-0.00 ± 0.16	73 ± 11	15000 ± 2400	828 ± 691	163 ± 25	9.74 ± 0.14
J2228+2201	56960	7840 ± 30	-1.72 ± 0.02	301 ± 7	7140 ± 210	-276 ± 64	62 ± 1	9.65 ± 0.03
	58693	2390 ± 10	-1.22 ± 0.01	145 ± 2	6080 ± 80	168 ± 28	95 ± 1	9.26 ± 0.01

Table 3. Continuum at 1450Å and C ɪᴠ spectral measurements for the three quasar considered in this work, at all observation epochs, as calculated by QSFit. *The C ɪᴠ line is very faint (with respect to the continuum), and the associated estimates are likely unreliable. For the emission-line velocity offsets, a positive value means the line is blueshifted. The last column shows the virial product calculated as $\nu L_\nu^{0.5} \times$ FWHM^2. **"~0.5 dex." Is this the uncertainty that applies to the virial product in the last column of Table 3? Or is this the uncertainty in the mass based on the scatter of the M-sigma relation? I recommend that the authors clarify this issue by writing a footnote in Table 3 and giving appropriate references to the literature therein.**

Dawson et al. 2013; Smee et al. 2013; Alam et al. 2015; Pâris et al. 2017) and the SDSS-IV Extended Baryon Oscillation Spectroscopic Survey (eBOSS; Dawson et al. 2016; Abolfathi et al. 2018; Pâris et al. 2018). These quasars were targetted via a range of techniques and algorithms (see Richards et al. 2002; Ross et al. 2012; Myers et al. 2015). The SDSS, BOSS, and eBOSS data are supplemented by spectra from the Low Resolution Imaging Spectrometer (LRIS; Oke et al. 1995) on the 10-m Keck I telescope and the Double Spectrograph (DBSP) instrument on the 200-inch Palomar Hale telescope.

MJG:: "(c) At the very end of section 2.3 the authors note that they use photometric measurements to set the absolute scale of the non-SDSS spectra. It would be useful to note here the resulting uncertainty in flux calibration and whether this uncertainty was propagated into measurements of the contin-

uum and emission lines from these spectra." Proper comparison of the spectra requires reliable flux calibrations, which is a challenge since not all data were taken in photometric conditions. SDSS spectra are spectrophotometrically calibrated. BOSS and eBOSS spectra have spectrophotometric corrections applied in the latest data release (Hutchinson et al. 2016; Jensen et al. 2016; Margala et al. 2016). However, some of the Palomar and Keck data suffered from variable conditions and clouds. For lower redshift AGN, the narrow [O ɪɪɪ] emission line is typically used to align spectrophotometry since it is spatially extended and not expected to change significantly on human timescales (e.g., Barth et al. 2011). However, due to the high-redshift of our quasars, [O ɪɪɪ] is not available to us to use for scaling the spectra. Instead, we use photometric data from ZTF since our Palomar and Keck data were all taken after MJD 57500. This provides broad-band photometry at the time of

QSFit takes into account, and propagates accordingly, the uncertainties in the spectrum.

the spectroscopy, which we use to scale the spectra whose initial calibration is based on spectrophotometric standards observed on the same nights. **MJG/NPR:: We note the resulting uncertainty in flux calibration is... [For the SDSS spectra,] this uncertainty was (not) propagated into measurements of the continuum and emission lines from these spectra....”**

2.4 Emission Line and Power-law Slope Measurements

We use the measured quasar emission line properties from several catalogues: Shen et al. (2011), Hamann et al. (2017), Kozłowski (2017), and Calderone et al. (2017).

In particular, we use the Quasar Spectral Fitting (QSFit) software package presented in Calderone et al. (2017). This provides luminosity estimates as well as width, velocity offset and EW of 20 emission lines, including C IV, C III] , and Mg II . We process and fit all nine spectra using the lastest version (v1.3.0) of the QSFit online calculator. The host galaxy and blended iron emission at rest-frame optical wavelengths components are automatically disabled when they can not be constrained by the available data, as is the case for all our quasars. Power-law continuum slopes, α, where $f_\lambda \propto \lambda^\alpha$, are also reported in these catalogues and from QSFit.

As described in detail in Calderone et al. (2017), the uncertainties in the measured quantities are determined by two methods; a Fisher matrix method and a Monte Carlo resampling method. Due to correlations among model parameters, e.g. emission-line luminosities and widths, the Fisher matrix method likely underestimates the errors.

Thus the Monte Carlo resampling method (Burtscher et al. 2009; Andrae 2010) is employed. This relies on the assumptions that the QSFit model provide a reliable representation of the data and that the uncertainties on the observed spectrum are Gaussian distributed with known standard deviation. QSFit is used to find the best-fitting model to the given spectral data. This best-fitting model is considered to be the ground truth but with no associated uncertainties. Using this 'ground truth', a set of mock spectra are generated whose flux, has a Gaussian distribtuion with standard deviation equal to the uncertainty of input data. The QSFit analysis is rerun these mock spectra, which are resampled 10^3 times, and the distribution of best-fitting parameters are reported. Section 2.8.3 and Appendix B4 of Calderone et al. (2017) gives further details and compares the Fisher matrix and Monte Carlo resampling uncertainties and distributions.

All of this is correct, but we didn't ran the Monte Carlo method, since the results would have been very similar to those obtained with the Fisher matrix method.
I would answer Referee's query as follows:
The parameters of the involved model components (a power-law for the continuum, and a single Lorentzian profile for the emission lines) show negligible correlations, hence we used the Fisher matrix method to estimate the uncertainties on the model parameters.

Figure 1 presents the optical and mid-infrared light curves for three high-redshift CLQ quasars. Figure 1 also indicates the spectra for each epoch with vertical dashed lines in the light curves.

Figure 2 shows the rest-frame spectra for SDSS J1205+3422. For J1205+3422, our spectral observations cover 5195 observed days, corresponding to 1691 days in the rest-frame. This quasar was initially identified in SDSS in 2005 May as a bright, $g \approx 18.0$, blue-sloped quasar with broad Si IV/O IV, C IV, C III, and Mg II. C III] and C IV have large blueshifts, $\approx 2600\pm150$ and $\approx 1150\pm100$ km s^{-1}, respectively. By 2019, however, the optical brightness dropped by nearly 2 magnitudes and the spectra are significantly less blue. Lyα and N V are detectable in both 2019 spectra, but is just blueward
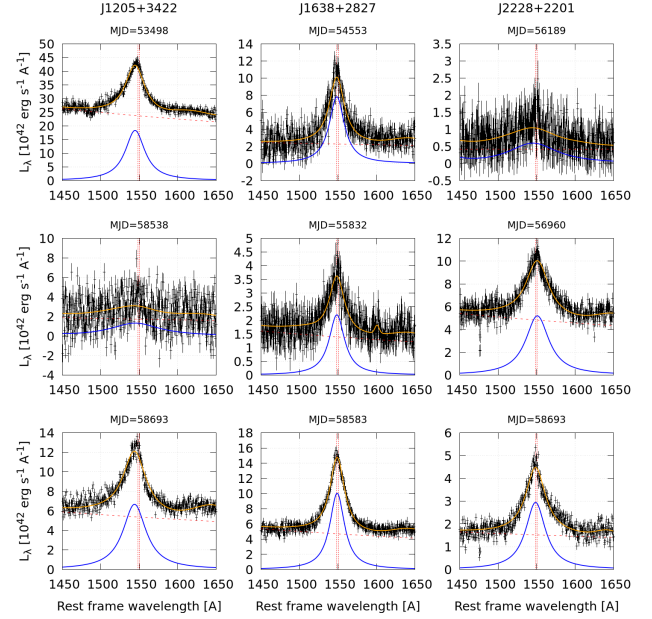
Figure 5. Observed spectra and best fit models of the C IV spectral region. The solid blue line is the Lorentzian profile fit to the C IV emission line. The long-dashed red line is the continuum fit, with the solid orange line giving the overall fit. The short-dashed vertical lines gives the rest wavelengths of the C IV doublet.

of the wavelength range covered by the original SDSS spectrum. The C IV and C III] lines have faded significantly between the SDSS observation in 2005 and the Palomar observations in 2019. Note that C IV is extremely faint in the 2019 February spectrum, but that night suffered from poor conditions.

Figure 3 shows the rest-frame spectra for SDSS J1638+2827. For J1638+2827, our spectral observations cover 4030 observed days, corresponding to 1265 days in the rest-frame. Here, in the initial epoch spectrum, C IV is broad and bright, as is C III. However, ≈ 400 rest-frame days later, the broad C IV and C III] emission lines have faded, the continuum slope around 1400Å has changed from ≈ -1.48 to ≈ -2.25, but the Lyα /N V emission complex is very similar in shape **and intensity**. Around 870 days in the rest-frame after the second spectral epoch, at the time of the third spectral epoch, the source has brightened from optical magnitudes of ~ 20 mag to ~ 18.5 mag. Lyα, N V, C IV, C III] , and Mg II are all apparent and broad, with Mg II being seen for the first time at high signal-to-noise. An absorption feature between Lyα and N V is seen in all three spectral epochs.

Figure 4 shows the rest-frame spectra for SDSS J2228+2201. For J2228+2201, our spectral observations cover 2504 observed days, corresponding to 778 days in the rest-frame. Over the course of 240 rest-frame days, C IV and C III] both *emerge* as BELs and **the standard UV/blue continuum becomes stronger.** Then, over the course of 538 days in the rest-frame, the broad emission, while still very present, reduces in line flux the UV/blue continuum diminishes. However, the third epoch still corresponds to a source more luminous than the initial BOSS spectrum.

3.2 C IV Emission Line Evolution

We analyzed the multi-epoch spectra of the three quasars using the QSFit spectral fitting package (Calderone et al. 2017). One advantage of using QSFit is that it allows constraints on the slope

We may follow two approaches here:
- identify (and justify) the proper values for E(B-V) and re-run the analysis. The numbers would change, but our conclusions concerning variability would not be affected;

- Change the text as follows:
All fits are performed assuming E(B-V) = 0 since, whatever the extnction is for each source, it would not change across epochs. Hence our results on each source variability would not be affected by considering the Milky Way extinction.

I would prefer the second, but we should not have mentioned E(B-V) in the text. Now that it's there, I'm afraid we must re-run the analysis.   The choice is up to you Nicholas.

and luminosity of the broad band continuum of the source. The relevant estimated quantities, including continuum luminosity and slope at rest-frame 1450Å, C IV line luminosity, FWHM, and EW are given in Table 3. All fits are performed with $E(B-V) = 0$ **Q: Is this the reddening intrinsic to the quasar or does it also include the reddening in the Milky Way? I presume the latter is known and could (and should) be corrected.** and the best fit models in the region of the C IV emission line are shown in Figure 5.

All C IV lines are fitted with a single, broad, Lorentzian profile. This allows us to account for the central peak of the C IV line. No additional narrow components are considered for several reasons. First, in the epochs of highest brightness, such a "narrow" component would have FWHM ~ 2000-3000 km s^{-1}, i.e. values exceeding the usual widths of genuine narrow lines ($\lesssim$ 1000 km s^{-1}). Second, allowing a second component to have such large widths would make that component highly degenerate with the "broad" components, causing the latter to have much larger widths, ~ 10,000 km s^{-1}. Finally, neglecting such a narrow component ensures a consistent model across all epochs.

Both the quasar continuum (evaluated at 1450Å), and the C IV line luminosities follow a similar evolution, with a ratio of ~20-30, confirming that the main driver for emission line variability is likely the broad band continuum itself. For all sources except J1638+2827, the slope of the continuum changes with luminosity following a "bluer-when-brighter" pattern, suggesting that a distinct emerging component is responsible for both the slope and luminosity variations. In J1638+2827 the opposite behaviour is observed, especially in the first observation epoch. However, this may be a bias due to the limited wavelength range available which extends to rest-frame $\lambda \sim 1240$ Å for the first epoch, while it extend to shorter wavelengths for the other epochs (respectively Å and 1010 Å). This suggests that the emerging component is more prominent at UV wavelengths, and a sufficient wavelength coverage is required to detect it. In all cases where the C IV line profile is reliably constrained, we find that the C IV FWHM is approximately constant with maximum variations $\lesssim$ 1000 km s^{-1}, despite significantly larger line luminosity variations.
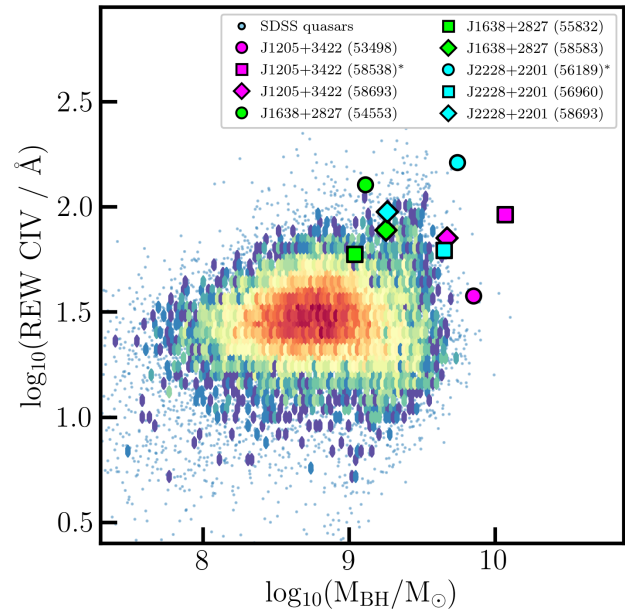
3.3 Virial Black Hole Masses

The FWHMs of quasar broad lines are related to the mass of the SMBH powering the quasar phenomenon, and that mass is assumed to be constant on any human timescale. Hence it is instructive to check whether the virial products, which are the basic quantity used to calculate single-epoch black hole mass estimates, show any variation. This approach assumes that the broad-line region (BLR) is virialized (e.g. Shen et al. 2011; Calderone et al. 2017). The continuum luminosity provides a proxy for the BLR radius, and the broad-line width (FWHM) provides a proxy for the virial velocity. This "virial mass" estimate is then expressed as:

$$\log(M_{BH}) = (\gamma L_\nu)^\gamma \times (FWHM)^\delta \quad (1)$$

where $\gamma = 0.5$ and $\delta = 2$. **This equation, as written, appears to be wrong because the LHS is a log while the RHS is not and there should be constants or calibration factors to connect the black hole mass to the luminosity and FWHM combination. Moreover, the exponent of the luminosity is not exactly 0.5 according to empirical determinations.**. The virial product for the C IV CLQs is reported in the last column of Table 3. The uncertainty typically associated with single-epoch mass estimates is ~ 0.5 dex, implying that the virial products for our three high-redshift CLQs are all remarkably constant and compatible with single black hole

The correct equation is:
$\log(M) = \log \left[\left(\frac{\nu L_\nu}{10^{42} \{\rm erg\ s^{-1}\}} \right)^{0.5} \left(\frac{\rm FWHM}{10^3 \{\rm km\ s^{-1}\}} \right)^2 \right] + {\rm constant}$

Figure 6. Colored density cloud shows virial black hole masses of ≈20,000 $z > 1.5$ quasars from QSFit catalogue (Calderone et al. 2017) compared to their C IV rest-frame equivalent widths (REWs). Overplotted are the three high-redshift CLQs considered here: J1205+3422 (magenta), J1638+2827 (green), and J2228+2201 (cyan). The symbol shapes indicate the observation epoch, with the first, second, and third epochs denoted by circles, squares, and diamonds, respectively. As per Table 3, an asterisk in the inset box signifies that the C IV line for that quasar observation is very weak, likely making the associated estimates unreliable.

masses per source, even in those cases where the C IV estimates were deemed potentially unreliable. The object showing the largest variation is J2228+2201, though even that source only spans a range of 0.48 dex.

Shen et al. (2011) and Kozłowski (2017) report virial black hole masses based on Mg II and C IV for the SDSS/BOSS observations of our targets. For J1205+3422, Shen et al. (2011) report $\log(M_{BH,MgII}/M_\odot) = 9.55 \pm 0.05$ and $\log(M_{BH,CIV}/M_\odot) = 9.49 \pm 0.04$. We use the mean of five values — three from our three epochs and two from Shen et al. (2011) — to calculate an adopted SMBH mass of $\log(M_{BH,vir}/M_\odot) = 9.73$ for J1205+3422. J1638+2827 also has two virial mass measurements from Shen et al. (2011), as well as two measurements from Kozłowski (2017). The mean mass measurement adopted for J1638+2827 is $\log(M_{BH,vir}/M_\odot = 9.09$. For J2228+2201, there are two Kozłowski (2017) measurements, leading to a mean adopted mass of $\log(M_{BH,vir}/M_\odot = 9.37$. We use these mean SMBH masses when calculating the Eddington ratios.

From the virial mass estimates, all our objects have SMBH masses $M_{BH} > 10^9 M_\odot$. This is at the upper end of SMBH masses at all epochs, and towards the extreme of the mass distribution for $z \sim 2$ quasars. Figure 6 compares the C IV EW versus the virial

Point 3-c by the Referee:
same as above: we are not interested in the correct calibration (as different authors use different ones...) but only if the virial product change significantly across epochs. Hence we may:
- drop any reference to \gamma, \delta and calibrations, and stress that we are interested in variabilities;
- read the papers mentioned by the Referee, check the ranges for such \gamma and \delta factors, compute the virial product for all combinations of such values, and check whether there is any appreciable change (beyond 0.5 dex).
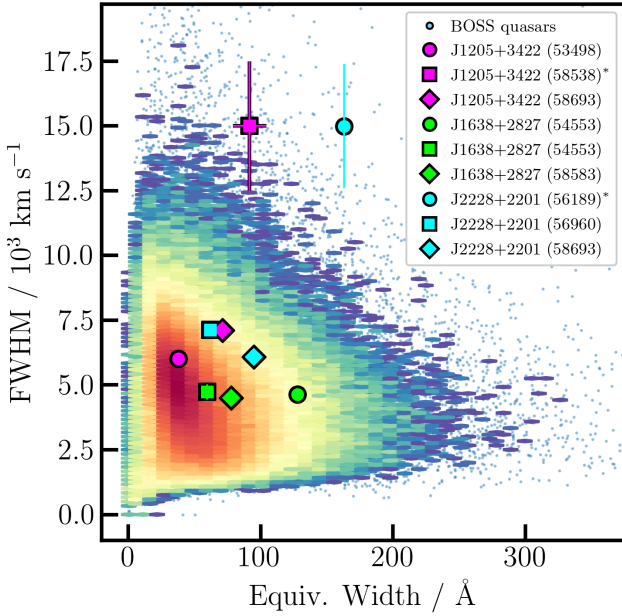
Point 3-d:
The quoted uncertainties account only for the propagation of uncertainties in the continuum luminosities and line widths. However, typical uncertainties associated to single epoch virial mass are $\sim$~0.5 dex, hence...

Point 3-e:
What is the figure whose font should be made bigger?

Figure 7. Rest-frame EW vs. FWHM of C IV for BOSS DR12 quasar sample (Hamann et al. 2017). Symbols as in Figure 6.

Object	MJD	$L_{\rm bol}$	$\eta_{\rm Edd}$
	53498	47.22	−0.61
J1205+3422	58538	46.07	−1.76
	58693	46.57	−1.26
	54553	46.17	−1.03
J1638+2827	55832	45.98	−1.21
	58583	46.50	−0.69
	56189	46.23	−1.24
J2228+2201	56960	47.34	−0.12
	58693	46.83	−0.64

Table 4. Bolometric luminosities are given in either Shen et al. (2011) or Kozłowski (2017) for the three CLQs. We scale these values using our measured νL_ν continuum luminosity values. From Section 3.3, we assume: $\log(M_{\rm BH,vir}/M_\odot) = 9.726$ for J1205+3422; $\log(M_{\rm BH,vir}/M_\odot) = 9.091$ for J1638+2827, and $\log(M_{\rm BH,vir}/M_\odot) = 9.366$ for J2228+2201. The Eddington luminosity $L_{\rm Edd} = 1.26 \times 10^{38} (M_{\rm BH}/M_\odot)$ erg s^{-1} and $\eta_{\rm Edd}$ is the log of the Eddington ratio.

2019; Hamann et al. 2017). Figure 7 shows the rest-frame EW versus the FWHM of the C IV emission line in the BOSS DR12 quasar sample from the catalogue of Hamann et al. (2017). Other than the two low quality, suspect observations, the multi-epoch observations of our high-redshift CLQs are all consistent with the bulk of the BOSS DR12 sample.

The temporal evolution of the velocity offsets, 1450 Å continuum luminosity, continuum slope, C IV line width (FWHM), and virial black hole mass estimates are shown in Figure 8. The C IV velocity offsets are approximately constant, and generally compatible with a single value (within 3σ). The exception is J2228+2201, where a significant change ($\sim 7\sigma$) is observed between the second and third epochs. The velocity blueshifts ($\sim 200 - 1100$ km s^{-1}) are consistent with rest-frame UV spectra of quasars over the redshift range $1.5 \leq z \leq 7.5$ (e.g., Meyer et al. 2019).

3.5 The C IV Baldwin Effect

The Baldwin effect (Baldwin 1977) is an empirical relation between quasar emission line rest-frame EWs and continuum luminosity (e.g., Shields 2007; Hamann et al. 2017; Calderone et al. 2017). Hamann et al. (2017) and Calderone et al. (2017) present recent measurements of the Baldwin effect for large quasar samples.

There is an anti-correlation between the rest-frame EWs and, e.g., 1450 Å rest-frame continuum luminosity, so that as the underlying UV continuum luminosity increases, the EW decreases. Figure 9 shows this for a sample of 20,374 quasars from the QSFit catalogue (Calderone et al. 2017). The slope is $\beta = -0.20$, consistent with Kozłowski (2017, $\beta = -0.25$, but for bolometric luminosity rather than rest-frame UV continuum luminosity) and with Hamann et al. (2017, $\beta = -0.23$).

We add the measurements from the three C IV CLQ at each epoch to Figure 9. All three quasars at all three epochs lie on the edge of the νL_ν-EW distribution. Also, with the exception of J1638+2827 on MJD 55832, all the measurements show an *intrinsic* Baldwin effect (e.g., Goad et al. 2004; Rakić et al. 2017). Subject to small number statistics, the slope of the intrinsic Baldwin effect for these three high-redshift C IV CLQs is somewhat steeper than the population trends, with $\beta \approx -0.38$, shown by the dashed red line in Figure 9.

4 DISCUSSION

4.1 Continuum and Line Changes: Comparisons to recent Observations

The top row of Figure 8 demonstrates that both the 1450 Å continuum and the C IV emission lines can exhibit large, greater than an order-of-magnitude, changes in luminosity, *and* that these continuum-line changes track each other.

Trakhtenbrot et al. (2019) report on the quasar 1ES 1927+654 at $z = 0.02$, which was initially seen to lack broad emission lines and line-of-sight obscuration, i.e, it was a "type 2" quasar. This object was then seen to spectroscopically change with the appearance of a blue, featureless continuum, followed by the emergence of broad Balmer emission lines — i.e., this quasar changed into a broad-line, or "type 1" quasar, after the continuum luminosity brightened. This implies that there is (at least in some cases) a direct relationship between the continuum and broad emission lines in CLQs. Many other examples of a similar phenomenon have been reported, albeit not with the dense spectral cadencing of 1ES 1927+654. A similar scenario may have occurred for the three high-redshift CLQs presented here, although we lack the high-cadence, multiwavelength, multi-epoch coverage that Trakhtenbrot et al. (2019) present. Interestingly, Trakhtenbrot et al. (2019) find no evidence for broad UV emission lines in their source, including neither C IV, C III] , nor Mg II . The authors attribute the lack of broad UV emission lines to dust within the BLR.

MacLeod et al. (2019) present a sample of CLQs where the primary selection requires large amplitude ($|\Delta g| > 1$ mag, $|\Delta r| > 0.5$ mag) variability over any of the available time baselines probed by the SDSS and Pan-STARRS1 surveys. They find 17 new CLQs, corresponding to $\sim 20\%$ of their observed sample. This CLQ fraction increases from 10% to roughly half, as the rest-frame 3420 Å continuum flux ratio between repeat spectra increases from 1.5 to 6 — i.e., more variable quasars are more likely to exhibit large changes in their broad emission lines. MacLeod et al. (2019) note
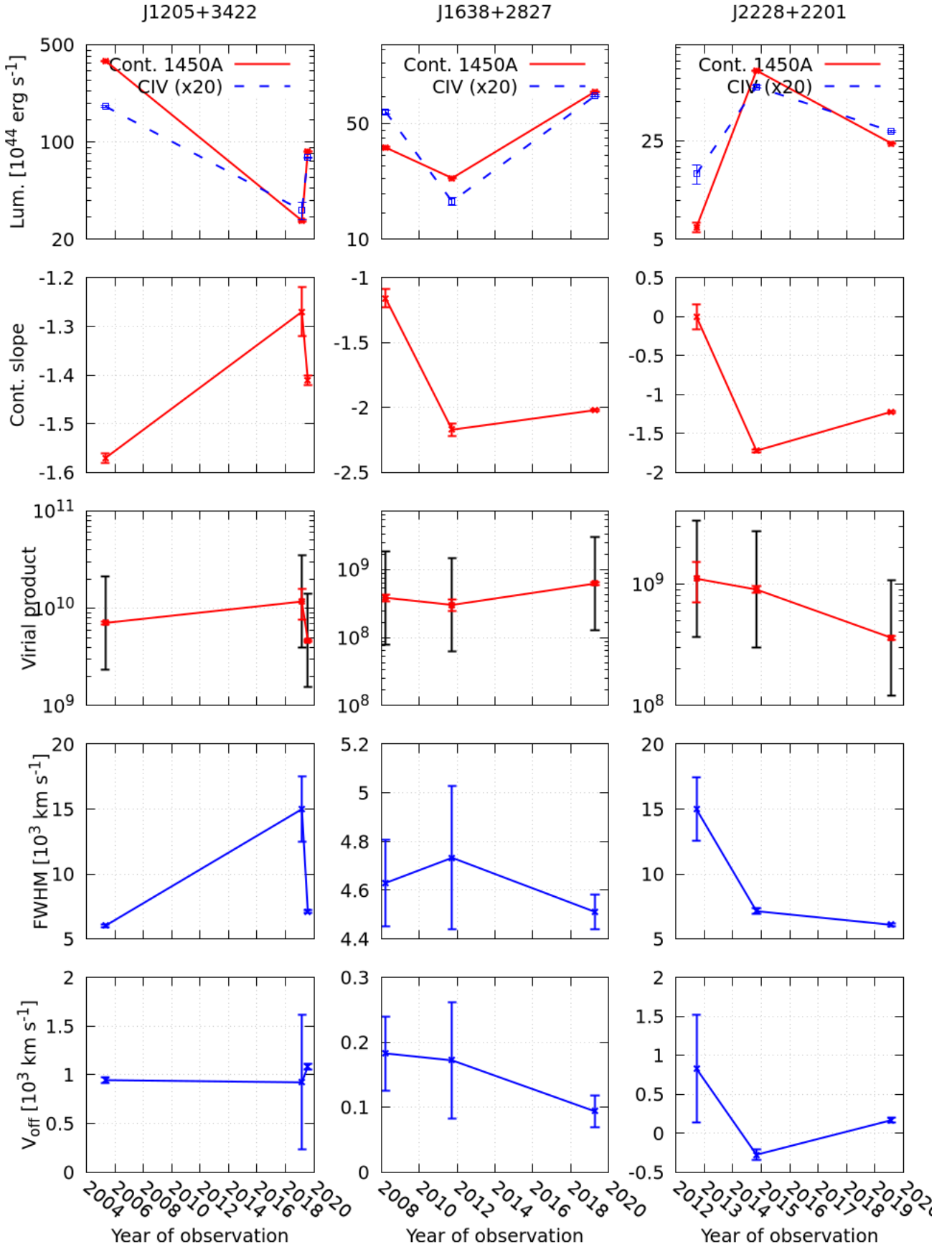
Figure 8. Temporal evolution of the spectral properties of the three quasars considered in this work.
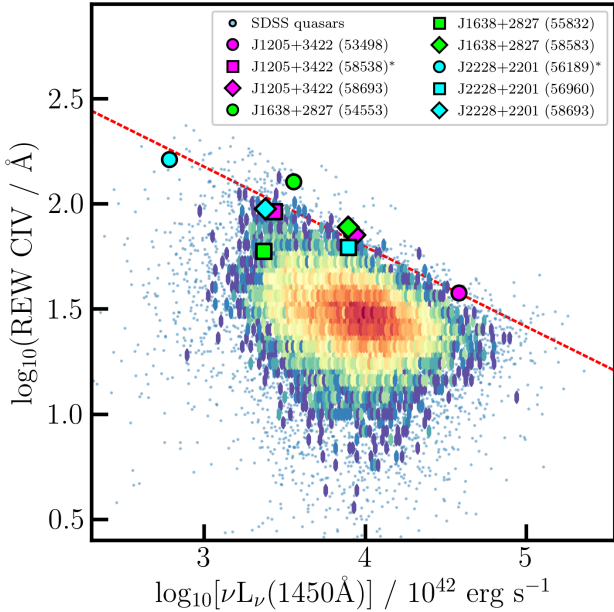
Figure 9. C IV equivalent width versus underlying continuum luminosity, commonly referred to as the Baldwin plot. The continuum luminosities are from Calderone et al. (2017). The rest-frame EW (REW) measurements are from Table 3. Symbols as in Figure 6. The dashed red line has slope $\beta = -0.38$.

that their CLQs have lower Eddington ratios relative to the overall quasar population.

Using the same dataset as MacLeod et al. (2019), Homan et al. (2019) investigate the responsiveness of the Mg II broad emission line doublet in AGN on timescales of several years. Again focussing on quasars that show large changes in their optical light-curves, Homan et al. (2019) find that Mg II clearly does respond to the continuum. However, a key finding from Homan et al. (2019) is that the degree of responsivity varies strikingly from one object to another. There are cases of Mg II changing by as much as the continuum, more than the continuum, or very little at all. In the majority (72%) of this highly variable sample, the behaviour of Mg II corresponds with that of Hβ. However, there are also examples of Mg II showing variations while but Hβ does not, and vice versa.

Graham et al. (2020) report the largest number of Hβ CLQs to date, with a sample of 111 sources identified. Graham et al. (2020) find that this population of extreme varying quasars, referred to as CSQs in their paper, is associated with *changes* in the Eddington ratio rather than simply the magnitude of the Eddington ratio itself. They also find that the timescales imply cooling/heating fronts propagating through the disk.

4.2 Continuum and Line Changes: Comparisons to Theoretical Expectations

The C IV line is one of the strongest collisionally excited lines in quasar spectra (e.g., Hamann & Ferland 1999). **Early measurements from e.g., Pogge & Peterson (1992) and Peterson (1997), using the well-studied Seyfert galaxy NGC 5548, suggested the location of C IV emission was produced by the innermost disk, with the line emission responding to the underlying continuum emission in only a matter of ~ 8 days. as indicated by reverberation mapping time-delay measurements. However, more re-**

cent measurements from e.g. Grier et al. (2019, and references therein), suggest that the lag between the C IV line and the continuum are of order > 100 observed-frame days. which would place the C IV emitting region far from the inner accretion disk. Importantly, many quasars in the Grier et al. (2019) sample are of comparable redshift and luminosity to SDSS J1205+3422, J1638+2827, and J2228+2201.

In standard Shakura & Sunyaev (1973) thin disk models, large changes in the continuum flux are not permitted over short timescales due to the relatively long viscous time associated with such disks. Given the observed short timescale continuum variations, we must consider more complex models. We note that two of our sources (J1205+3422 and J2228+2201) have C IV EW and continuum luminosity changes which fall comfortably along a line, implying their variation is consistent with an intrinsic Baldwin effect (see Figure 9). **The light-crossing time of the region that produces the C IV line is substantial, which translates into a delay between the variations of the continuum and the C IV line, and a smoothing of the light curve of the latter. Thus, if the excitation of the C IV line is driven by the changes in the continuum, the excited gas cannot reach an equilibrium excitation state as quickly as the continuum changes.** This makes the slope of the intrinsic Baldwin effect greater than that of the overall ensemble slope, which is derived from many single-epoch observations, the majority of which are assumed to be in equilibrium. **Grier et al. (2019),**

The presence of an intrinsic Baldwin effect implies those sources may comfortably fit into the sample of C IV variable quasars explored by Dyer et al. (2019). Similar to those authors, we consider slim accretion disk models (e.g., Abramowicz et al. 1988), which may explain the observed variability. In particular, the summary of disk variation timescales presented in Stern et al. (2018) shows that timescales are shorter for taller disks, permitting changes similar to those observed if they are caused by heating or cooling fronts propagating on the disk sound crossing time. Dyer et al. (2019) also consider inhomogeneous disk models (e.g., Dexter & Agol 2011) where flux variations are driven by azimuthal inhomogeneities in the temperature of the disk. Such inhomogeneities could arise from disk instabilities (e.g., Lightman & Eardley 1974) or interactions of embedded objects (e.g., McKernan et al. 2014, 2018). If an inhomogeneous disk is responsible for the continuum variations, which then drive C IV variations, it implies that our objects are simply the extreme outliers produced by a process which occasionally, but rarely, produces very large hot or cool spots. The frequency of such occurrences can be used to constrain the slope and normalization of the power law distribution of spot size.

Finally, we must also consider the disk/wind model which has successfully reproduced many features of quasar C IV observations, notably the common blueshifted offset (e.g., Murray et al. 1995). In this model, C IV is optically thick at low velocities, but optically thin at high velocities, with $\tau \sim 1$ at ~ 5000 km s^{-1}. In a disk/wind model, the BLR is very small, implying short timescales of emission line variability. Also in this model, there should be associated strong absorption in the soft X-ray band, which could be tested with follow-up observations.

The foregoing discussion directly applies to the two objects which maintain an intrinsic Baldwin effect relationship between C IV EW and continuum luminosity. However, J1638+2827 clearly does not maintain such a relationship — indeed, the continuum and C IV EW appear somewhat correlated, rather than anti-correlated, in this source. This implies that the illumination of the C IV emitting region by a variable ionising continuum and the corresponding

change in the photoionisation state alone cannot explain the collapse and recovery of the line.

4.3 Eddington Ratios and State Changes

The broad UV and optical lines in quasars are most sensitive to the extreme ultraviolet (EUV) part of the SED, with C IV (and indeed He II and N V) being at the higher energy end of the EUV distribution.

Noda & Done (2018) note that the soft X-ray excess – the excess of X-rays below 2 keV with respect to the extrapolation of the hard X-ray spectral continuum model, and a common feature among Type 1 AGN – produces most of the ionizing photons, so its dramatic drop can lead to the disappearance of the broad-line region, driving the changing-look phenomena. Noda & Done (2018) go on to make a connection between state changes in Galactic binaries and CLQs. In Galactic binaries spectral hardening corresponds to the soft-to-hard state transition in black hole binaries, which occurs at $L/L_{\rm Edd} \sim 0.02$ (i.e., $\eta_{\rm Edd} \sim -1.7$). During this state transition, the inner disc evaporates into an advection-dominated accretion flow, while the overall drop in luminosity appears consistent with the hydrogen ionisation disc instability. Noda & Done (2018) predict that changing-look AGNs are similarly associated with state transitions at $L/L_{\rm Edd}$ of a few percent.

Comparing observed correlations between the optical-to-X-ray spectral index (i.e., $\alpha_{\rm ox}$) and Eddington ratio in AGN to those predicted from observations of X-ray binary outbursts, Ruan et al. (2019) find a remarkable similarity to accretion state transitions in prototypical X-ray binary outbursts, including an inversion of this correlation at a critical Eddington ratio of $\sim 10^{-2}$, i.e., at the same ratio motivated by Noda & Done (2018). These results suggest that the structures of black hole accretion flows directly scale across a factor of $\sim 10^{8}$ in black hole mass and across different accretion states. Using Ruan et al. (2019) as a guide, there are potentially three accretion regimes: *(i)* a "High/Soft State" with $\eta_{\rm Edd} \gtrsim -1$; *(ii)* a "Low/Hard State" with $-2 \lesssim \eta_{\rm Edd} \lesssim -1$; and *(iii)* a "Low/Hard State" with $\eta_{\rm Edd} \lesssim -2$. These are given as shaded regions in Figure 10.

Apart from J1205+3422 on MJD 58538, we see all the C IV CLQ epochs are above $L/L_{\rm Edd} \sim 5\%$. As we have noted throughout, the spectrum for J1205+3422 on MJD 58538 has low SNR, so while this object could well have entered a 'low-state', this is difficult to conclusively confirm. Nevertheless, and taking the J1205+3422 spectrum at face-value, we note that all the C IV CLQs are well above $\sim 1\%$ in Eddington luminosity and thus the suggested "Low/Hard State" boundary.

While we note there is interest in plotting these accretion rates, and motivation from Noda & Done (2018) and Ruan et al. (2019), we very much caution on over-interpretation at this juncture. The point of this paper was to report on three very interesting CLQs. Our object definitions are based on empirical, observed properties. The potential for physical connections of accretion physics across the large-range of mass-scales is tantalising, but is left to future investigations.

5 CONCLUSIONS

In this paper we have reported on three redshift $z > 2$ quasars with dramatic changes in their C IV emission lines, the first sample of changing-look quasars at high redshift. This is also the first time the changing-look behaviour has been seen in a high-ionisation emission line.

- SDSS J1205+3422, J1638+2827 and J2228+2201 show interesting behaviour in their observed optical light curves, and subsequent spectroscopy shows significant changes in the C IV broad emission line, with both line collapse and emergence being displayed on rest-frame timescales of $\sim 240 - 1640$ days.
- Where observed, the profile of the Lyα/N V emission complex also changes, and there is tentative evidence for changes in the Mg II line.
- Although line measurements from the three quasars show large changes in the C IV line flux-line width plane, the quasars are not seen to be outliers when considered against the full quasar population in terms of (rest-frame) EW and FWHM properties.
- We put these observations in context with recent "state-change" models, and note that with the exception of the low SNR spectrum of J1205+3422 on MJD 58538, even in their low state, the C IV CLQs are above $\sim 5\%$ in Eddington luminosity.

There are now more observed examples of dramatic, dynamic changes in supermassive black hole systems e.g. CLQs/CSQs than Galactic X-ray Binaries. While the timescales are expected to scale with black hole mass, whether the full physical system at large does, including the associated atomic physics, remains an open question.

Availability of Data and computer analysis codes

All materials, databases, data tables and code are fully available at: https://github.com/d80b2t/CIV_CLQs.

Figure 10. Eddington ratios of the three C IV CLQs. Grayscale gives the Eddington ratio ranges for quasars from SDSS Shen et al. (2011) and BOSS (Kozłowski 2017). Symbols as in Figure 6. The red region ($L/L_{\rm Edd} \approx 0.02 \pm 0.01$; $\eta_{\rm Edd} = -1.7 \pm 0.13$) is the transition accretion rate suggested by Noda & Done (2018). A "High/Soft State" with $\eta_{\rm Edd} \geq -1$ and a a "Low/Hard State" with $\eta_{\rm Edd} \leq -2$ are indicated with dashed lines and arrows.

REFERENCES

Abazajian K. N., et al., 2009a, ApJS, 182, 543
Abazajian K. N., et al., 2009b, ApJS, 182, 543
Abolfathi et al., 2018, ApJS, 235, 42
Abramowicz M. A., Czerny B., Lasota J. P., Szuszkiewicz E., 1988, ApJ, 332, 646
Alam S., et al., 2015, ApJS, 219, 12
Alloin D., Pelat D., Phillips M., Whittle M., 1985, ApJ, 288, 205
Antonucci R., 2018, Nature Astronomy, 2, 504
Astropy Collaboration et al., 2013, Astron. & Astrophys., 558, A33
Baldwin J. A., 1977, ApJ, 214, 679
Barth A. J., et al., 2011, ApJ Lett., 743, L4

Bellm E. C., et al., 2019a, PASP, 131, 018002
Bellm E. C., et al., 2019b, PASP, 131, 068003
Bian W.-H., Fang L.-L., Huang K.-L., Wang J.-M., 2012, MNRAS, 427, 2881
Calderone G., et al., 2017, MNRAS, 472, 4051
Cutri R. M. o., 2013, Technical report, Explanatory Supplement to the AllWISE Data Release Products. IPAC/Caltech
Cutri R. M., et al., 2011, Technical report, Explanatory Supplement to the WISE Preliminary Data Release Products. IPAC/Caltech
Dawson K., et al., 2013, AJ, 145, 10
Dawson K. S., Kneib J.-P., et al., 2016, AJ, 151, 44
Dexter J., Agol E., 2011, ApJ Lett., 727, L24
Doan A. N., et al., 2019, in American Astronomical Society Meeting Abstracts #233. p. 242.23
Drake A. J., et al., 2009, ApJ, 696, 870
Drake A. J., et al., 2013, ApJ, 763, 32
Dyer J. C., Dawson K. S., du Mas des Bourboux H., Vivek M., Bizyaev D., Oravetz A., Pan K., Schneider D. P., 2019, ApJ, 880, 78
Eisenstein D. J., Weinberg D. H., et al., 2011, AJ, 142, 72
Elvis M., 2000, ApJ, 545, 63
Fukugita M., Ichikawa T., Gunn J. E., Doi M., Shimasaku K., Schneider D. P., 1996, AJ, 111, 1748
Gerum R., 2019, arXiv e-prints, p. arXiv:1910.00279v2
Goad M. R., Korista K. T., Knigge C., 2004, MNRAS, 352, 277
Graham M. J., Djorgovski S. G., Drake A. J., Mahabal A. A., Chang M., Stern D., Donalek C., Glikman E., 2014, MNRAS, 439, 703
Graham M. J., et al., 2015a, MNRAS, 453, 1562
Graham M. J., et al., 2015b, Nat, 518, 74
Graham M. J., Djorgovski S. G., Drake A. J., Stern D., Mahabal A. A., Glikman E., Larson S., Christensen E., 2017, MNRAS, 470, 4112
Graham M. J., et al., 2019, PASP, 131, 078001
Graham M. J., et al., 2020, MNRAS, 491, 4925
Grier C. J., et al., 2019, ApJ, 887, 38
Guo H., Sun M., Liu X., Wang T., Kong M., Wang S., Sheng Z., He Z., 2019, ApJ Lett., 883, L44
Hamann F., Ferland G., 1999, ARA&A, 37, 487
Hamann F., et al., 2017, MNRAS, 464, 3431
Hemler Z. S., et al., 2019, ApJ, 872, 21
Homan D., Macleod C. L., Lawrence A., Ross N. P., Bruce A., 2019, arXiv

e-prints, p. arXiv:1910.11364

Hutchinson T. A., et al., 2016, AJ, 152, 205

Jensen T. W., et al., 2016, ApJ, 833, 199

Kaiser N., et al., 2010, in Society of Photo-Optical Instrumentation Engineers (SPIE). p. 0, doi:10.1117/12.859188

Kozłowski S., 2017, ApJS, 228, 9

Kramida A., Ralchenko Y., Reader J., NIST ASD Team 2018, doi:10.18434/T4W30F,

Kramida A., Yu. Ralchenko Reader J., and NIST ASD Team 2019, NIST Atomic Spectra Database (ver. 5.7.1), [Online]. Available: https://physics.nist.gov/asd [2019, November 7]. National Institute of Standards and Technology, Gaithersburg, MD.

LaMassa S. M., et al., 2015, ApJ, 800, 144

Lawrence A., 2018, Nature Astronomy, 2, 102

Leighly K. M., 2004, ApJ, 611, 125

Lightman A. P., Eardley D. M., 1974, ApJ Lett., 187, L1

MacLeod C. L., et al., 2012, ApJ, 753, 106

MacLeod C. L., et al., 2019, ApJ, 874, 8

Magnier E. A., et al., 2013, ApJS, 205, 20

Mahabal A. A., et al., 2011, Bulletin of the Astronomical Society of India, 39, 387

Mainzer A., et al., 2011, ApJ, 731, 53

Margala D., Kirkby D., Dawson K., Bailey S., Blanton M., Schneider D. P., 2016, ApJ, 831, 157

Masci F. J., et al., 2019, PASP, 131, 018003

Matthews T. A., Sandage A. R., 1963, ApJ, 138, 30

McKernan B., Ford K. E. S., Kocsis B., Lyra W., Winter L. M., 2014, MNRAS, 441, 900

McKernan B., et al., 2018, ApJ, 866, 66

Meyer R. A., Bosman S. E. I., Ellis R. S., 2019, MNRAS, 487, 3305

Murray N., Chiang J., Grossman S. A., Voit G. M., 1995, ApJ, 451, 498

Myers A. D., et al., 2015, ApJS, 221, 27

Noda H., Done C., 2018, MNRAS, 480, 3898

Oke J. B., Gunn J. E., 1983, ApJ, 266, 713

Oke J. B., et al., 1995, PASP, 107, 375

Pâris I., Petitjean P., Ross N. P., et al., 2017, Astron. & Astrophys., 597, A79

Pâris I., et al., 2018, Astron. & Astrophys.

Peterson B. M., 1997, An Introduction to Active Galactic Nuclei

Pogge R. W., Peterson B. M., 1992, AJ, 103, 1084

Proga D., Stone J. M., Kallman T. R., 2000, ApJ, 543, 686

Rakić N., La Mura G., Ilić D., Shapovalova A. I., Kollatschny W., Rafanelli P., Popović L. Č., 2017, Astron. & Astrophys., 603, A49

Richards G. T., et al., 2002, AJ, 123, 2945

Richards G. T., et al., 2011, AJ, 141, 167

Ross N. P., et al., 2012, ApJS, 199, 3

Ross N. P., et al., 2015, MNRAS, 453, 3932

Ross N. P., et al., 2018, MNRAS, 480, 4468

Ruan J. J., Anderson S. F., Eracleous M., Green P. J., Haggard D., MacLeod C. L., Runnoe J. C., Sobolewska M. A., 2019, arXiv e-prints, p. arXiv:1903.02553v1

Schneider D. P., et al., 2010, AJ, 139, 2360

Shakura N. I., Sunyaev R. A., 1973, Astron. & Astrophys., 24, 337

Shen Y., et al., 2011, ApJS, 194, 45

Shen Y., et al., 2015, ApJS, 216, 4

Shen Y., et al., 2019, ApJS, 241, 34

Shields J. C., 2007, in Ho L. C., Wang J. W., eds, Astronomical Society of the Pacific Conference Series Vol. 373, The Central Engine of Active Galactic Nuclei. p. 355 (arXiv:astro-ph/0612613)

Smee S. A., et al., 2013, AJ, 146, 32

Stern D., et al., 2017, ApJ, 839, 106

Stern D., et al., 2018, ApJ, 864, 27

Stoughton C., et al., 2002, AJ, 123, 485

Stubbs C. W., et al., 2010, ApJS, 191, 376

Sun M., Xue Y., Richards G. T., Trump J. R., Shen Y., Brandt W. N., Schneider D. P., 2018, ApJ, 854, 128

Taylor M. B., 2005, in Shopbell P., Britton M., Ebert R., eds, Astronomical Society of the Pacific Conference Series Vol. 347, Astronomical Data Analysis Software and Systems XIV. p. 29

Taylor M., 2011, TOPCAT: Tool for OPerations on Catalogues And Tables, Astrophysics Source Code Library (ascl:1101.010)

The Astropy Collaboration et al., 2018, preprint, (arXiv:1801.02634v2)

Tonry J. L., et al., 2012, ApJ, 750, 99

Trakhtenbrot B., et al., 2019, ApJ, 883, 94

Wilhite B. C., Vanden Berk D. E., Brunner R. J., Brinkmann J. V., 2006, ApJ, 641, 78

Wright E. L., et al., 2010, AJ, 140, 1868

York D. G., et al., 2000, AJ, 120, 1579

Zakamska N. L., et al., 2016, MNRAS, 459, 3144

Zakamska N. L., et al., 2019, MNRAS, 489, 497

This paper has been typeset from a TEX/LATEX file prepared by the author.